Structure induced reversible anionic redox activity in Na layered oxide cathode

Xiaohui Rong[1,†], Jue Liu[2,†], Enyuan Hu[3,†], Yijin Liu[4], Yi Wang[1], Jinpeng Wu[5], Xiqian Yu[1,*], Katharine Page[2], Yong-Sheng Hu[1,*], Wanli Yang[5], Hong Li[1], Xiao-Qing Yang[3], Liquan Chen[1] and Xuejie Huang[1]

1 Beijing National Laboratory for Condensed Matter Physics, Institute of Physics, Chinese Academy of Sciences, School of Physical Sciences, University of Chinese Academy of Sciences, Beijing 100190, China

2 Chemical and Engineering Materials Division, Oak Ridge National Laboratory, Oak Ridge, TN 37831, USA

3 Chemistry Division, Brookhaven National Laboratory, Upton, NY 11973, USA

4 Stanford Synchrotron Radiation Lightsource, SLAC National Accelerator Laboratory, Menlo Park, CA 94025, USA

5 Advanced Light Source, Lawrence Berkeley National Laboratory, Berkeley, CA 94720, USA

*Corresponding author: xyu@iphy.ac.cn; yshu@iphy.ac.cn

† R.X.H., J. L. and E. H. contribute equally to this paper.

Abstract

The utilization of redox activities on oxygen, namely the anionic redox reaction (ARR), is one way to increase the capacity of layered cathode oxides for lithium ion and sodium ion batteries. However, how structures response to such ARR and to what extent oxygen can be reversibly oxidized is still under debate. Here a P3-type $Na_{0.6}[Li_{0.2}Mn_{0.8}]O_2$ with reversible capacity from pure ARR was studied. The detailed crystal structure of the desodiated phase was solved, showing the structure is very stable against oxygen release. The inter-layer O-O pair (2.506(2) Å), associated with oxidization of oxygen anions, was directly detected by using neutron total scattering for the first time. The formation of O-O pair (or peroxo like O-O dimer, ~2.5 Å) is usually observed in lithium

rich compounds with 4d or 5d transition metals (e.g. Ru and Ir) and its stabilization is thought to be related to the strong metal-oxygen (M-O) covalent bonding in those systems. For P3-type $Na_{0.6}[Li_{0.2}Mn_{0.8}]O_2$ with relatively weak Mn-O covalent bonding, crystal structure factors could play an even more important role in stabilizing the oxidized species, as both Li and Mn ions are immobile in the structure and thus may inhibit the transformation of the oxidized species to O_2 gas. Structure refinements of neutron and X-ray total scattering data show there is almost no oxygen vacancy in charged (4.5V) sample, indicating there is almost no structure oxygen loss after initial charging, and confirming that the current structure has strong structural stability towards the oxidized oxygen ions. These results suggest an alternative route to promote the reversible ARR by tuning the crystal structure other than introducing strong M-O covalent bonds.

Introduction

Layered transition metal oxide compounds (AMO_2, A=Li^+ or Na^+, M=transition metal ions) are important positive electrode materials for rechargeable Li-ion and Na-ion batteries, owing to their compact crystal structure and thus has the ability to realize high energy density. In classical scenarios, charge compensation of these compounds upon alkali ions (Li^+ and Na^+) intercalation/deintercalation is simultaneously balanced by reduction/oxidation of transition metal species (such as Mn, Co and Ni), and lithium or sodium storage capacities depend solely on the cationic redox reactions.[1-5] However, this rule has been challenged with the discovery of the lithium rich (or Li excess) layered transition metal oxides (nominal composition of $Li[Li_xM_{1-x}]O_2$, M = 3d, 4d or 5d transition metal ions) used for positive materials of Li-ion batteries.[6,7] Lithium rich layered transition metal oxides possess similar structure to that of α-$NaFeO_2$ typed $LiCoO_2$, a commercialized layered positive electrode material for Li-ion batteries, with the replacement of a portion of transition metal ions by lithium ions in the transition metal layers.[8-10] These materials display abnormally high reversible capacity exceeding 280mAh g^{-1} (above 4.5V vs. Li^+/Li), which cannot be simply explained by cationic redox reactions occurring on transition metal ions.[3,9,11] Numerous research work has

thus been performed to investigate the charge compensation mechanisms associated with the high capacity, and consensus has been reached that oxygen anions do participate in the charge compensation in addition to the cationic redox reactions.[7,12-18] However, how oxygen anions participate in the charge compensation and how the structure responds to such anionic activities is still under fierce debate. Early reports by Dahn suggested that the loss of oxygen from the crystal lattice upon a high degree of delithiation led to the high capacity,[8,12] and oxygen gas evolution has been directly observed in Li-rich oxides during the first charge process by Bruce and other groups with the differential electrochemical mass spectrometry (DEMS) technique.[19] In 2005, long before the Li-rich oxides cathode materials were reported, Yoon *et al*. presented the soft X-ray absorption spectroscopy (s-XAS) results, indicating that oxygen holes were formed to compensate the charge balance upon removal of Li^+ in regular $LiNi_{0.33}Co_{0.33}Mn_{0.33}O_2$ (NCM) layered material.[20] Most recently, Bruce *et. al* investigated Li-rich NCM typed $Li_{1.2}[Ni_{0.13}Co_{0.13}Mn_{0.54}]O_2$ material through a combination of s-XAS, Raman and resonant inelastic X-ray scattering (RIXS) techniques, and confirmed the formation of localized oxygen hole (O^-) without O-O dimerization. They believed this accounts for the extra reversible capacity observed in Li rich oxides.[17] Tarascon and co-workers reported the direct observation of peroxo-like O-O dimers (~2.5Å) in delithiated Li_2IrO_3, a lithium rich oxide with 5d transition metal ion, with the help of atomic-resolution scanning transmission electron microscopy (STEM) technique and powder neutron diffraction.[15] The oxidization of oxygen anions resulted in the formation of peroxo-like species which may be stabilized through a metal-driven reductive coupling mechanism. The reversibility of oxo- to peroxo-like transformation ($2O^{2-}/(O_2)^{n-}$), namely the anionic redox reactivity, is tightly related to the covalent bonding nature of M(d)-O(p) as demonstrated by lithium rich oxides with 4d or 5d transition metal.[16] Ceder *et al*. proposed that a specific local lithium rich environment in lithium rich oxides is a prerequisite for oxygen to participate in redox reaction and contribute to high capacity. They also stressed that the covalence of M(d)-O(p) does not lead to a higher capacity than that is expected from transition metals alone.[18] It is agreed that both the composition and structural

complexity of the lithium rich compounds makes the distinguishing of anionic redox activities difficult, and key experiments or new approaches remain to be performed.

Recently, Goodenough and co-workers reported a P3-type $Na_{0.6}[Li_{0.2}Mn_{0.8}]O_2$, displaying promising reversible capacity (3.5V-4.5V vs. Na^+/Na) as a positive electrode material for Na-ion batteries.[21] Since Mn (Mn^{4+}) ions are not likely to get oxidized or reduced in the voltage range of cycling, anionic redox reaction on oxygen is likely to be the only accountable resource for the observed reversible capacity. In addition, manganese/lithium ions are unlikely to be able to migrate to the interlayer sites due to the size mismatch between the transition metal site and sodium site (and thus the structural complexity is further removed), making this material ideally suited for a fundamental study of the anionic redox relativities in layered oxide materials. However, Nazar et al. then reported a P2-type $Na_{0.6}[Li_{0.2}Mn_{0.8}]O_2$ which was synthesized in a different method. Nevertheless, it has a totally different electrochemical performance with that of P3-type $Na_{0.6}[Li_{0.2}Mn_{0.8}]O_2$, and the former does not show a remarkable discharge plateau at ~4.0V as P3-type $Na_{0.6}[Li_{0.2}Mn_{0.8}]O_2$ does. This result indicates that structure plays an important role in these materials of anionic redox class.[22] In this work, X-ray and neutron total scattering (both Bragg diffraction and diffuse scattering), hard and soft X-ray absorption spectroscopy (hXAS and sXAS), X-ray photoelectron spectroscopy (XPS) and transmission X-ray microscopy (TXM) techniques were employed, to study the local and average structural evolution as well as the charge compensation mechanisms of P3-type $Na_{0.6}[Li_{0.2}Mn_{0.8}]O_2$ upon charge and discharge. Using the neutron PDF technique, we show the first direct experimental evidence of the formation of O-O pairs with short distance of ~2.5 Å, associated with the oxidization of oxygen anions in desodiated P3-type $Na_{0.6}[Li_{0.2}Mn_{0.8}]O_2$. The structural origins of the reversible oxygen redox activity are also discussed. In the following sections, unless otherwise indicated, $Na_{0.6}[Li_{0.2}Mn_{0.8}]O_2$ is of P3-type.

Results and discussion

Structure of P3-type $Na_{0.6}[Li_{0.2}Mn_{0.8}]O_2$. The major diffraction peaks of the

synchrotron XRD pattern can be indexed using the layered P3-type structure (S.G. *R*3m). At least two other minor phases have been identified: a layered P2-type structure in S.G.$P6_3/mmc$ and a β-$NaMnO_2$ in S.G. *P*mmn. Extra weak diffraction peaks are found between d = 3.0 Å and d = 5.0 Å, which may be attributed to the super lattice diffraction peaks associated with the in *ab*-plane ordering of Li and Mn. This assessment is further supported by the disappearance of these weak diffraction peaks in corresponding neutron diffraction patterns due to the much smaller coherent nuclear scattering length difference between Li (*b* = -1.9 fm) and Mn (*b* = -3.7 fm). It is also worth noting that in *ab*-plane Na^+/vacancy ordering may also exist in the current compound, driven by the 2:1 composition ratio between Na^+ and vacancies. Details in plane ordering schemes falls out of the scope of the current study and will be reported elsewhere. Rietveld refinement was carried out against both synchrotron XRD and neutron powder diffraction. The refinement result confirms that the layered P3-type phase is indeed the dominant phase with a weight fraction of about 90%. The refinement results are shown in Table 1, Figure 1, Figure S1 and Table S1, and the refined chemical composition is $Na_{0.58}Mn_{0.83}Li_{0.17}O_2$. It can be seen that the oxygen ions follow the AABBCC… stacking sequence. Na^+ ions reside on the interlayer trigonal prismatic sites formed by adjacent layer oxygen ion arrays with the same stacking sequences (A-A, B-B or C-C). The P3-type phase is found to be easily converted to the P2-type phase at high synthetic temperature due to their structure similarity. Thus, it is difficult to synthesize the phase pure P3-type $Na_{0.6}[Li_{0.2}Mn_{0.8}]O_2$ using conventional high temperature solid state synthesis. However, it is worth noting that the capacity contribution from the minor P2-type phase (less than 10%) is very limited and should not affect the current study.

Electrochemical performance of $Na_{0.6}[Li_{0.2}Mn_{0.8}]O_2$/Na half cell. The electrochemistry performance of $Na_{0.6}[Li_{0.2}Mn_{0.8}]O_2$ was evaluated in sodium half cells. The charge-discharge curves at current rates of 0.1 C (10 mAg^{-1}) and 2.0 C (200 mAg^{-1}) of the first cycle of $Na_{0.6}[Li_{0.2}Mn_{0.8}]O_2$ are plotted in Figure 2a. The coin cells were tested in the voltage range of 3.5-4.5 V vs. Na/Na^+. Under the current rate of 0.1 C, the

typical initial discharge capacity is ~80 mAh g^{-1}, the initial average discharge voltage is 4.0 V. While the initial discharge capacity at 2.0 C rate is ~90% of that at 0.1 C without optimization. The result indicates that $Na_{0.6}[Li_{0.2}Mn_{0.8}]O_2$ has outstanding rate capability, though the polarization becomes larger at high C-rate.

The cycling performance at different current rates is shown in Figure 2b (for 0.1C vs. 2.0C) and Figure S2 (for 0.3C). The cycling performance at 2.0C is even better than that at 0.1 C, which shows higher coulombic efficiency (75% at 2.0C and 67% at 0.1 C for the initial cycle; 99% at 2.0 C and 96% at 0.1 C for the following cycles) and less capacity decay after 50 cycles.

Structural evolution upon Na^+ de-intercalation/intercalation. To investigate the structural evolution of $Na_{0.6}[Li_{0.2}Mn_{0.8}]O_2$ upon Na^+ de-intercalation and intercalation, in operando XRD measurement was carried out on $Na_{0.6}[Li_{0.2}Mn_{0.8}]O_2$/Na cell charged/discharged in the voltage range of 3.5V and 4.5V (Figure 3). The evolution of the XRD patterns displays the remarkable two-phase reaction feature with the disappearance of one set of diffraction peaks and the appearance of another set of diffraction peaks. The desodiated phase can also be indexed using a P3 layered structure with *R*3m space group, indicating the oxygen stacking sequence is likely to be maintained and the global crystal structure is relatively stable upon the de-intercalation of Na^+. Due to the relatively poor signal-to-noise ratio of the lab XRD patterns collected *in situ*, *ex situ* measurements were performed to accurately determine the crystal structure of the samples at charged and discharged states. Additionally, it is worth noting the presence of appreciable amounts of stacking faults in the charged (4.5 V) sample, as evidenced by the very asymmetrical and broad diffraction peaks in both neutron and synchrotron X-ray diffraction data (Figure S3). Therefore, to accurately resolve the atomistic structure of the charged sample, it is imperative to quantitatively model the stacking faults, a task that we shall discuss in details in the following section.

Structure of charged (4.5V) and discharged (3.5V) samples. While Bragg diffraction provides detailed information about the average structure, the detection of local structure features such as the peroxo like O-O dimer (if it is localized), requires a local

probing tool to detect. The real-space based PDF utilizes both the Bragg diffraction and diffuse scattering signal and thus is highly sensitive to the local distortion and chemical short range ordering.[23-27] Therefore, both X-ray PDF (xPDF) and neutron PDF (nPDF) data were collected for the pristine and charged $Na_{0.6}[Li_{0.2}Mn_{0.8}]O_2$ sample and the results are displayed in Figure 4. The xPDF results of pristine and charged samples are shown in the bottom line of Figure 4, displaying similar peak shape and peak position for the first neighbor Mn-O and Mn-Mn correlations. This agrees well with the conclusion from XRD that Na^+ extraction doesn't incur significant changes in transition metal framework.

While X-ray scattering is very sensitive to heavy atoms such as Na and Mn and thus can effectively detect the transition metal framework, it has relatively poor sensitivity towards light atoms such as oxygen. Therefore, it is imperative to collect high quality neutron total scattering data to gain direct insights about the local and average oxygen environments in the charged/discharged samples. Since C-C double bonds and C-F bonds have similar bond length as the peroxide bonds (~1.5 Å), it is desired to use pure active material (P3-type $Na_{0.8}Mn_{0.8}Li_{0.2}O_2$ here) without any conductive carbon or polymer binder for the current investigation to avoid potential ambiguities. Indeed, we found it is possible to reproduce normal charge/discharge curves without adding binder to the electrode. However, attempts to remove carbon additives have failed so far, presumably due to the poor electronic conductivity of this compound (relative to the layered transition metal oxides such as $LiCoO_2$ or $NaCoO_2$). Therefore, the final electrodes used for the current study contain 5% (mass ratio) carbon and 95% active material. For the neutron PDF analysis, corresponding amounts of carbon signal were removed from all collected data (to obtain difference PDF), as can be seen in Figure S4. This approach has been proven to be effective as evidenced by the very similar refinement results (Figure S5 and Table S2) between the pure pristine sample (without carbon) and the pristine electrode (5% carbon) with the removal of carbon signal. The local neutron PDF of the pristine sample, sample recovered from the charge state (4.5 V) and discharge state (3.5 V) are shown in Figure 4 and Figure S4. A very weak intensity increase can be seen for the peak around 1.5 Å, indicating that very limited O-

O peroxide pair, if it exists, in the charged sample. In clear contrast, the original 2.637 (4) Å O-O pair (inter O-O distance in the $Mn(Li)O_6$ octahedra) in the pristine sample shift to much shorter distance ~ 2.506(3) Å, similar to the observation in the charged Li_2IrO_3.[15] It is also worth noting that the $G(r)$ peak intensity associated with Na-O bonds (~2.4Å) decreases dramatically after charging, indicating that Na has been effectively removed. This assessment is further supported by the increase of the $G(r)$ peak intensity at ~3.2 Å due to the decrease of the negative intensity contribution from the closest Na-Mn pairs. The $G(r)$ intensity of the charged sample becomes much weaker at larger atomic pair distances (> 10 Å) relative to the pristine sample, indicating either the formation of much smaller particles or the introduction of large amounts of disorder. More interestingly, almost all $G(r)$ peaks can be recovered to that of the pristine data after discharging to 3.5V (Figure S4). This is in clear contrast to many lithium-rich transition metal oxides where clear irreversible phase transitions have been observed after the first cycle.[8-10] This observation also proves that the lattice oxygen in this P3-type compound is relatively rigid and can effectively stabilize the reduced oxygen ions. The presence of large amounts of stacking faults and the relatively large particle size of the charged sample makes it difficult to carry out quantitative structure analysis using only PDF data.[23,26] Therefore, the reciprocal space neutron and X-ray total scattering data were first used for the structure refinements of the charged samples (later, this model has also been applied to the modeling of neutron PDF data). Refinement details can be found in experimental part. The refinement results are shown in Figure 5, Table S3 and Table S4. It can be seen that about 4% (mass ratio) carbon are refined in the charged and discharged samples, a value that is very similar to the experimental results (during the electrode preparation). The refined oxygen site occupancy for the initial charged sample (4.5 V) is near unity (occO1 = 0.99(5), occO2 =1.00(7)), indicating that there is almost no structure oxygen loss (in the bulk material) after initial charging. This is distinct from what has been observed in lithium rich compounds where a considerable amount of oxygen vacancies are usually created due to the loss of oxygen at high voltage charging, confirming that the current structure has strong structural stability towards the oxidized oxygen ions. This assumption is further supported by the excellent

structure reversibility for the initial discharge sample (3.5 V), and the low concentration of oxygen vacancy refined for the second (cycle) charged sample (occO1 = 0.94(6), occO2 =0.95(7)). The observed apparent charge/discharge plateaus (unlike the slopes for most lithium-rich materials) may also be rooted in this excellent structure stability upon oxygen reduction/oxidation. X-ray PDF (Figure S6) results shows that after 20 cycles, the electrode sample still shows good crystallinity as pristine sample, by *ex-situ* SEM (Figure S7 and S8) of the electrode, there are not distinct differences between the pristine and cycled electrode particles. These results supports that the material has good structure stability and the capacity decay should not be attributed to the previously suspected amorphous phase.[21]

Spectroscopic results and charge compensation mechanism. Tarascon and coworkers have demonstrated that XPS is an effective tool to identify the oxygen related species,[15] the O1s XPS experiments were carried out and the results are displayed in Figure 6a. These spectra can be decomposed into several components, which have been identified as signals from oxygen crystalline network (529.5eV), CO_3^{2-} or oxygenated deposited species (531.5eV) and hydroxyl-like species (~533eV) respectively. The new component at ~530.5 eV corresponding to the per-oxo like species is appears/disappears in spectrum of charged/discharged electrodes, further proving the occurrence of reversible oxygen redox reactivity upon electrochemical cycling.

The charge compensation mechanisms of $Na_{0.6}[Li_{0.2}Mn_{0.8}]O_2$ upon Na^+ de-intercalation and intercalation were investigated by various spectroscopic techniques. The hard Mn K-edge X-ray absorption near edge spectroscopy (XANES) results are shown in Figure 6b. The XANES spectra do not show an entire edge shift but change in the edge shape, indicating the valence state of Mn remains unchanged upon charge/discharge and the de-intercalation/intercalation of Na^+ only causes the changes in coordinating environment. Unlike the complicated XANES shape changes often observed in other manganese based oxides, an "isosbestic point" feature[17,28,29] is revealed in $Na_{0.6}[Li_{0.2}Mn_{0.8}]O_2$, suggesting a two-phase reaction mechanism during de-intercalation/intercalation of Na^+. Since the transition metal L-edge which represents

the electric dipole-allowed 2p-3d transition is relatively intense and sensitive to the transition metal d orbital, Mn L-edge XAS experiments were performed to further confirm the valence state of Mn (Figure 6c). The two main peaks at the L_{III} and L_{II} edges, which are due to the respective electronic transitions from the metal 2p3/2 and 2p1/2 core levels to an unoccupied 3d level, are not significantly changed in shape and position for all spectra. This suggests the Mn ions do not change the valence state and thus do not participate in the charge-compensation during charge and discharge processes. Soft X-ray O K-edge absorption spectra are also collected on a series of $Na_{0.6}[Li_{0.2}Mn_{0.8}]O_2$ electrodes at different electrochemical states, as shown in Figure S9. The pre-edge features in O K-edge XAS represents the Mn-O hybridization states. Contrast between the O K-edge XAS of the pristine and the charged (1^{st} charged to 4.5V) samples was previously used as evidence of Oxygen redox [Cite Ref 17 Peter bruce paper here if you want]. Detailed discussions on the O-K XAS are out of the scope of this paper, but we would like to note that the lineshape and intensity of these features are largely determined by Mn-O hybridization, therefore, the hybridization feature change in O K-edge XAS does not provide conclusive evidence for oxygen redox.

Chemical and morphological evolution on sample particles. Two-dimensional nanoscale XANES mapping measurements were performed to investigate the Mn oxidation states in particles with different charge/discharge state (SOC/SOD) as well as different cycling history. The reflection point (edge energy) of the XANES spectrum at each pixel of the XANES mapping was used to determine the oxidation state of Mn. The local spectra over arbitrarily selected pixels are shown in the Figure S10. The similarity in the overall color of the particles shown in the top row of Figure 7 suggests the homogeneity of the Mn's oxidation states regardless of the SOC/SOD and the cycling history up to 30 cycles. The corresponding histograms of the edge energy over the highlighted particles are presented in the bottom row. Gaussian fitting suggests the variation of the edge energy (the FWHM of the fit) over the highlighted particles is between 0.7 eV and 1.3 eV, which is nearly at the energy resolution limit of 1 eV of the

instrument used in this study. The average value of edge energy is very close to that of MnO_2, indicating the oxidation state of Mn ions remain at $Mn^{4+}$for all investigated sample particles. This is significantly different from that observed in manganese based lithium rich layered oxides (e.g. $Li_2Ru_{0.5}Mn_{0.5}O_3$) where Mn^{4+} ions are reduced along surface and internal cracks due to release of oxygen gas upon high voltage charging. The three-dimensional transmission X-ray tomography (TXM) images of pristine and cycled sample particles were also collected (Figure S11). The cycled $Na_{0.6}[Li_{0.2}Mn_{0.8}]O_2$ sample particle looks very dense, in contrast to lithium rich layered oxides which show increase in porosity after prolonged electrochemical cycling.[30]

Discussion

The spectroscopic results show that Mn ions remain at Mn^{4+} over the entire charge and discharge process of $Na_{0.6}[Li_{0.2}Mn_{0.8}]O_2$ in the voltage range of 3.5V-4.5V (vs. Na^+/Na). The Mn cation doesn't participate in the charge compensation and the oxygen redox reaction contributes solely to the observed reversible capacity. Unlike other lithium rich oxides showing consecutive cationic and anionic reaction upon charging and discharging, $Na_{0.6}[Li_{0.2}Mn_{0.8}]O_2$ displays reversible capacity solely from the redox activities on oxygen, guarantying it a perfect system to study the anionic redox action. According to our *in situ* XRD results, the oxidation of oxygen anions (O^{2-}) occurs in the bulk structure, not only on the surface as indicated by Du *et.al*.[17,31] The *ex situ* experimental results show that the charged $Na_{0.6}Li_{0.2}Mn_{0.8}O_2$ is highly air and moisture sensitive, and is readily to be re-intercalated and converted back to the pristine phase. (Figure S12) Therefore, sample preparations with extreme caution are essential for *ex situ* measurements.

The short O-O distance of around 2.5 Å, associated with the oxidization of oxygen anions (O^{2-}), is directly detected by using neutron PDF (nPDF), a tool with the power to provide direct probing of real-space structure. The refinements of the crystal structure using reciprocal space total scattering data further support the decrease of inter-layer O-O distance (Figure 5). The presence of such short O-O distance, arising from the formation of peroxo like species (O_2^{n-} with O-O distance of ~ 2.5 Å), was theoretically

predicted and experimentally confirmed through HRTEM and neutron powder diffraction in the recent studies of Li_2IrO_3, a family of lithium rich oxide compounds with the 5d transition metal of Ir.[15] The stabilization of the short peroxo like O-O bond was explained by Tarascon *et. al* via. a reductive coupling mechanism, that is the covalent M-O bonding can stabilize the electrons on the oxygen hole by delocalizing them over M-O and O-O bonds. Otherwise, the oxygen dimer will be de-coordinated from the metallic network and released from the lattice as O_2 gas. In that scenario, the strong covalency of the M-O (e.g. Ir-O) bond is essential to stabilize the peroxo like O-O dimer and thus promotes promote the reversible redox reaction with lattice oxygen. For compounds with weak covalent M-O bond, such as Li_2MnO_3 ($Li[Li_{1/3}Mn_{2/3}]O_2$), oxygen gas is readily released upon first charging, resulting in irreversible structural changes and severe capacity fade or/and voltage fade. However, the P3-type $Na_{0.6}[Li_{0.2}Mn_{0.8}]O_2$ exhibits surprisingly high reaction reversibility associated with the redox reaction of oxygen, implying that other factors may play an important role in enhancing the reversible oxygen redox activities. Chen and Islam investigated the dynamic process of the rearrangement of the oxygen network in Li_2MnO_3 upon delithiation.[32] Based on their DFT calculations, the delithiation will drive the progressive formation of peroxo like O-O dimer (<2.5 Å), peroxide O-O dimer (O_2^{2-} 1.5 Å), superoxide O-O dimer (O_2^- 1.3Å), and ultimately neutral oxygen dimer (O_2, 1.21 Å). The entire process is thermodynamically favorable, and therefore peroxo/peroxide like O-O dimer is undoubtedly formed but in a transient state. The formation and transformation of the peroxide O-O dimer will trigger the migration of Mn ions, and these two processes are intimately correlated. In light of the crystal structure of P3-type $Na_{0.6}Li_{0.2}Mn_{0.8}O_2$, the trigonal prismatic Na site is larger relative to the octahedral site (Mn/Li) in transition metal layers, and the size of the vacant site formed in between is not suitable for the migration of Mn and Li to alkali ion (Na) layers. This assessment has been further confirmed by the structure refinement using neutron total scattering data of the charged sample (Figure 5). The immobile nature of the cations in transition metal layers poses resistance for the reorganization of the oxygen network to generate O_2 gas, and therefore stabilizes peroxo like dimers or

oxygen holes in the structure. In addition, unlike the lithium rich oxide compounds which usually show the "S" shape of voltage profiles after the first charging process, [ref. X. Yu, AEM, 2014, 4, 1300950] the P3-type $Na_{0.6}Li_{0.2}Mn_{0.8}O_2$ displays both charge and discharge plateaus in extended cycling. Ceder *et al*. have recently shown that the high capacity as well as the voltage plateau is due to the special "O-Li-O" configuration associated with the lithium rich environment in the transition metal layers.[18] The invariant Li-O local environment, rooted in the immobile nature of cations in TM layers of P-type $Na_{0.6}Li_{0.2}Mn_{0.8}O_2$, explain the well preserved charge and discharge plateaus over the battery cycling. These results suggest an alternative way to promote the reversible anionic redox reaction by tuning the crystal structure, so as to increase the reversible capacity of lithium rich cathode oxides.

The neutron PDF pattern shows a slight increase (though relatively weak for quantitative analysis) in intensity for the peak located at ~1.5Å. This result indicates that the existence of peroxide O-O (1.5Å) bond cannot be excluded in the structure of the charged $Na_{0.6}Li_{0.2}Mn_{0.8}O_2$, which needs to be further confirmed. The rationalization of the formation of the peroxide O-O dimer in transition metal oxide has been demonstrated by Chen and Wang in the study of anatase TiO_2 and rutile TiO_2 *via.* DFT calculations.[33] Their results indicate that the O-O dimerization is energetically more favorable than separated oxygen holes in anatase TiO_2, in contrast to the situation in rutile TiO_2 with a relatively compact structure. They claimed that the large void space in the anatase structure may tolerate large structural distortion associated with O-O dimerization and concluded that the formation of the peroxide O-O dimer may be universal in a series of transition metal oxides with specific structure. As for the present case of $Na_{0.6}[Li_{0.2}Mn_{0.8}]O_2$, the large size of the trigonal prismatic Na site also gives a thicker interlayer in the P-type structure relative to that in the O-type structure (i.e. Li_2MnO_3, alkali ions occupy the octahedral site), providing enough void space to enable the dimerization of O-O to a deeper extent without incurring significant structural rearrangement or phase transformation. Other experimental proofs are being pursued to further consolidate this argument.

It is worth noting that $Na_{0.6}[Li_{0.2}Mn_{0.8}]O_2$ shows significant capacity fade upon the electrochemical cycling. E*x situ* X-ray PDF (Figure S6), inductively coupled plasma atomic emission spectrometry (ICP-AES, Table S5), electrochemical impedance spectroscopy (EIS, Figure S13) and *ex situ* XPS (Figure S14 and Table S6) measurements were performed to understand the fading mechanism. Based on these experimental results, the capacity fade is likely due to that the Na ions cannot fully intercalated into the structure after multiple charge-discharge cycles. (Figure S6 and Table S6) There are two main issues may cause this problem: (1) the creation of defects or cracks due to the internal strain caused by the phase transformation, leading to the creation of "dead area" due to the loss of electronic contract; However, such micro-structure changes didn't incur significant chemical and morphological changes in particles as indicated by TXM (spatial resolution ~50nm), as confirmed by SEM observations as well; (2) growth of the SEI. The extensive side reactions between the possible oxygen species and the electrolyte give rise to continuous accumulation of the SEI layer on the electrode surface, resulting in rapid buildup of overall cell impedance (as shown in Figure S13) and may impede the sodium diffusion locally. Therefore, nano-engineering or surface coating might be an effective way to improve the cycle performances of this material. In addition, the capacity of this material also needs further improvement. A practical way is to increase the sodium content in the sodium layer, and broadening the voltage cutoffs (introducing the Mn^{4+}/Mn^{3+} redox couple) is another enforceable strategy as well. Further attempts to design and synthesize P3 type manganese based layered oxides with increased capacity and improved cycle performances are on the way.

Conclusion.

In summary, the spectroscopic results confirm that the reversible capacity observed in P3-type layered $Na_{0.6}[Li_{0.2}Mn_{0.8}]O_2$ cycled in the voltage range of 3.5-4.5V (vs. Na^+/Na) originates from the redox activities on oxygen anions exclusively. The redox reaction on oxygen anions causes reversible global crystal structure change as indicated by *in situ* XRD measurement. The oxidation of oxygen anions leads to the formation of O-O

pairs (~2.5 Å), which was detected by nPDF directly for the first time. Such short O-O pair (peroxo like dimers), firstly observed in Li_2IrO_3, was previously explained to be stabilized in the cationic network through strong metal-oxygen covalent bonding. For $Na_{0.6}[Li_{0.2}Mn_{0.8}]O_2$ with weak Mn-O covalent bonding, structural factors seem to play an even more important role in stabilizing the oxidized oxygen species (e.g. dimer, oxygen hole) in the structure. Characterizing the oxygen related global and local structural features and exploring their relevance to electrochemical behaviors will be vitally important for better design of layered oxide positive materials with higher reversible capacity. Finally, this work illustrates that the neutron PDF is undoubtedly a powerful tool to probe both the average and local structural features associated with light elements (e.g. Li, O), and will be relevant to the study of anionic redox reaction mechanisms for many other layered oxide electrode materials.

Experimental

Materials synthesis

P3 type $Na_{0.6}[Li_{0.2}Mn_{0.8}]O_2$ was prepared by a solid-state reaction using precursor of Na_2CO_3 (99.9%, Alfa), LiOH (98%, Alfa), MnO_2 (99.9%, Alfa). The starting materials were weighed and ground in an agate mortar according to the appropriate stoichiometric ratio (2% more Na_2CO_3 and LiOH were used because of the volatilization loss during the process). Then the mixture was pressed into a pellet under a pressure of 10 MPa and the pellets were heated at 700^{o}C for 24 h in air atmosphere and cooled to room temperature naturally. The heating and cooling rates of the powders were 4^{o}C and ~2^{o}C min^{-1}, respectively.

Electrochemical measurements

All the electrochemical tests were conducted using coin cells (CR2032), assembled in an argon filled glove-box. The working electrode was prepared by rolling out the mixture of active material (80 wt%), Super P (15 wt%) and Polytetrafluoroethylene (PTFE 5 wt%) into thin films, followed by cutting into equal-area pieces and drying at 120 ^{o}C in vacuum for 10 hours. The loading mass of active material on positive electrode was controlled to between 6.0–7.0 mg/cm^{-2}. The electrolyte was a solution of

1 M $NaClO_4$ in ethylene (EC), dimethyl carbonate (DMC), propylene carbonate (PC) (1: 1 :1 in volume) and fluoroethylene carbonate (2% in volume). Sodium foil was used as the counter electrode and glass fiber was used as the separator. The charge and discharge tests were carried out using a Land CT2001A battery test system (Wuhan, PR China) in a voltage range of 3.5–4.5 V at various C-rates at room temperature.

Material Characterization

Lab XRD/SEM The structure was characterized using an X'Pert Pro MPD X-ray diffractometer (XRD) (D8 Bruker) with Cu-K_α radiation (λ= 1.5405Å) in the scan range (2θ) of 10-80^o. The morphologies of the samples were investigated by scanning electron microscopy (SEM, Hitachi-S4800). The specific ratios of Na, Li and Mn in the samples were measured by inductively coupled plasma atomic emission spectrometry (ICP-AES). In the *in situ* XRD studies, the working electrode was prepared using polyvinylidene fluoride (PVDF) as binder on an Al foil. A specially designed Swagelok cell equipped with an X-ray-transparent aluminum window was used for the *in situ* measurements. The *in situ* XRD patterns were collected with an interval of 40 min for each 2θ scan from 10^o to 60^o on charge and discharge at a current rate of 0.1C, between 3.5 ~ 4.5 V versus Na/Na^+. For all *ex situ* characterizations, the cells were disassembled at different states of charge and discharge, and the cathode was washed three times in dimethyl carbonate (DMC) before drying, assembled in an argon filled glove-box. Extreme caution should be paid when dealing with the charged sample to prevent any contact with air/moisture, as it is very easy to convert the material back to the discharged (or pristine) phase as shown in Figure S8.

XPS The X-ray photoelectron spectroscopy (XPS) spectra were recorded with a spectrometer having Mg/Al K radiation (ESCALAB 250 Xi, ThermoFisher). All binding energies reported were corrected using the signal of the Super P at 284.4 eV as an internal standard. All the samples were protected from air and moved to the detector cavity by the transfer equipment provided by ThermoFisher.

Synchrotron radiation XRD/PDF

Synchrotron X-ray diffraction experiments were carried out using beamline 17-BM-B (λ = 0.72768 Å) at the Advanced Photon Source at Argonne National Laboratory. PDF

experiments were carried out at the XPD beamline (beamline ID28) at the National Synchrotron Light Source II (NSLS-II, BNL, USA), with a photon wavelength of 0.185794Å. The diffraction patterns collected from 2D detector were radially integrated using Fit2D.[23,34,35] The pair distribution functions, G(r), were extracted using PDFgetX 3.[23,35,36]

Neutron diffraction/PDF Powder neutron scattering data were collected at the NOMAD beamline at the Spallation Neutron Source (SNS) at Oak Ridge National Laboratory. About0.115 g powder samples (carbon, pristine sample with/without carbon, sample charged to 4.5 V with carbon, discharged to 3.5 V with carbon and sample recharged to 4.5 V with carbon) were loaded into 3 mm quartz capillaries. Two 30 min scans were collected for each powder sample and they were then summed together to improve the statistics. The detectors were calibrated using a diamond powder standard prior to the measurements. Neutron powder diffraction data were normalized against a vanadium rod, the background was subtracted, and the total scattering structure factor S(Q) data were transformed to pair distribution function data G(r) using the specific IDL codes developed for the NOMAD instrument.[37] The Q range used for the Fourier transform is 0.2 $Å^{-1}$ to 28 $Å^{-1}$. Small box (unit-cell based) refinements were carried out in the TOPAS software (version 6).[36]

Stacking faults refinements Numerical stacking faults refinements of the charged samples (to 4.5 V) were carried out in TOPAS software (version 6) using neutron and synchrotron X-ray diffraction data.[35,38] A single layer $Na_{0.2}Mn_{0.8}Li_{0.2}O_2$ (three layers in the P3-type phase) was used as the basic repeat unit for the supercell construction, as can be seen in Figure 5. The in basal (*ab*) plane symmetry was strictly obeyed by placing atoms on the special sites. The initial translation vectors were all set to be (2/3, 1/3, 1) to satisfy the symmetry requirements of P3-type phase (*R*3m). A 15-layer supercell was used for the refinement (it was found that further increase of the layer number would not significantly improve the final R_{wp} value).

hXAS and sXAS *Ex situ* hXAS experiments were performed at beamline BL14W at Shanghai Synchrotron Radiation Facility (SSRF, Shanghai, China) in transmission mode with a Si (111) double-crystal monochromator detuned to the 35% value of its

original maximum intensity to eliminate the higher-order harmonics. The reference spectrum was simultaneously collected for energy calibration by using a reference metal foil. *Ex situ* sXAS measurements were carried out at beamline BL08U1A at SSRF and beamline 8.0 at Advanced Light Source (ALS, USA) in partial electron yield (PEY) mode. X-ray Absorption Near Edge Structure (XANES) data was analyzed by the ATHENA software package.

Synchrotron X-ray imaging For TXM imaging experiments, X-rays were monochromatized by a double Si (111) monochromator (energy resolution at ~1 eV) and focused by a capillary condenser for illumination of the sample. A Fresnel zone plate with 200 microns diameter and 30 nm outermost zone width was used as an objective lens that projects the image to the CCD detector. The effective pixel size is about 33.1 nm and the typical single exposure is set at 0.5 seconds. For the 3D morphological study, full tomographic data that covers -90 to 90 degrees with angular step at 0.5 degrees was acquired with incoming X-rays of 8500 eV. In addition to the sufficient photon counts and the fine angular steps, the quality of the reconstruction is further enhanced by adapting an iterative tomographic algorithm known as the Algebraic Reconstruction Technique (ART).[39-41] For the TXM XANES measurements, the full field imaging was coupled with the energy scan across the Mn absorption edge. Projection images with and without the sample were collected at more than 100 energy points across the Mn K-edge. The reference image correction, image registration, XANES spectra normalization and analysis, tomographic reconstruction were performed using an SSRL in-house developed software package known as the TXM-Wizard.[42,43]

Author contributions

Y.-S.H. and X.Y. designed this work; R.X.H., J. L. and E. H. contribute equally to this paper; R.X.H. carried out the electrochemical experiments; R.X.H. performed *in situ* XRD; J.L., E.H., K.P. and X.Y. performed *ex situ* XRD, xPDF, nPDF measurements and structural analysis; R.X.H., Y.W., W.J.P and Y.W.L. performed XPS, hXAS and

sXAS measurements; X.Y., W.J.P and Y.W.L. performed hXAS and sXAS analysis; X.Y. and Y.L. carried out TXM experiments; Y.L. performed TXM analysis; X.Y., R.X.H., J.L. and Y.-S.H. wrote the paper; all the authors participated in analysis of the experimental data and discussions of the results as well as preparing the paper.

Acknowledgement

The work in Beijing National Laboratory for Condensed Matter Physics was supported by funding from ‘973’ Projects (2014CB932300), the NSFC (11234013 and 51421002), and One Hundred Talent Project of the Chinese Academy of Sciences. Research conducted at the NOMAD beamline at ORNL’s Spallation Neutron Source was sponsored by the Scientific User Facilities Division, Office of Basic Sciences, U.S. Department of Energy. The work at Brookhaven National Laboratory was supported by the U.S. Department of Energy, the Assistant Secretary for Energy Efficiency and Renewable Energy, Office of Vehicle Technologies through Advanced Battery Material Research (BMR) program under Contract No. DE-SC0012704. This research used resources 28-ID-2 of the National Synchrotron Light Source II, a U.S. Department of Energy (DOE) Office of Science User Facility operated for the DOE Office of Science by Brookhaven National Laboratory under Contract No. DE-SC0012704. The authors would like to acknowledge that the research used Beamline 17-BM at the Advanced Photon Source (Contract No. DE-AC02-06CH11357) and BL14W, BL08U1A at Shanghai Synchrotron Radiation Facility. This research used resources of Beamline 8.0.1 of the Advanced Light Source (ALS), which is a DOE Office of Science User Facility under contract no. DE-AC02-05CH11231.

Additional information

The authors declare no competing financial interests. Correspondence and requests for materials should be addressed to X.Y. and Y.-S.H.

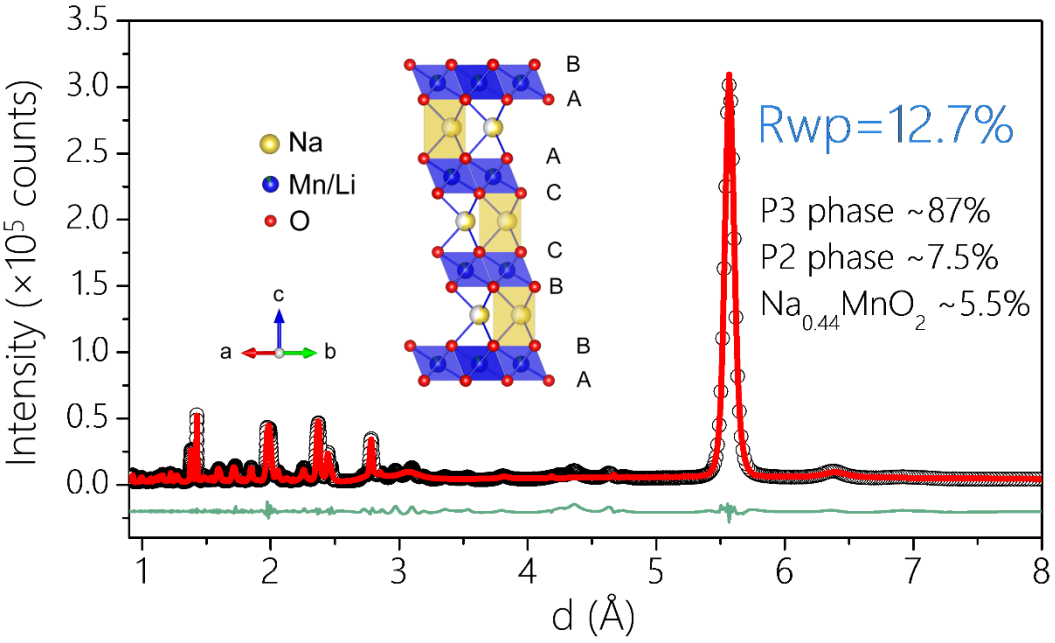

Figure 1 Crystal structure of the pristine $Na_{0.6}[Li_{0.2}Mn_{0.8}]O_2$. XRD pattern (λ = 0.24129 Å) of the as prepared $Na_{0.6}[Li_{0.2}Mn_{0.8}]O_2$. The inset shows the structure of $Na_{0.6}[Li_{0.2}Mn_{0.8}]O_2$ material with the P3 stacking. The sodium, manganese, lithium and oxygen atoms are shown in yellow, blue, green and red, respectively.

Table 1 Crystal structure of $Na_{0.6}Li_{0.2}Mn_{0.8}O_2$ refined from neutron diffraction data.

Space group *R*3m		***a* = 2.8433(14) Å, *c* =16.642(9) Å**				
Atom	**Wyck.**	***x***	***y***	***z***	**Occ.**	**B_{eq} (Å^2)**
Na1	4a	0	0	01752(7)	0.58(3)	2
Mn1	4a	0	0	0	0.83(1)	0.4
Li1	4a	0	0	0	0.17(1)	2
O1	4a	0	0	0.3987(8)	1	0.61(7)
O2	12b	0	0	0.6080(7)	1	0.51(2)

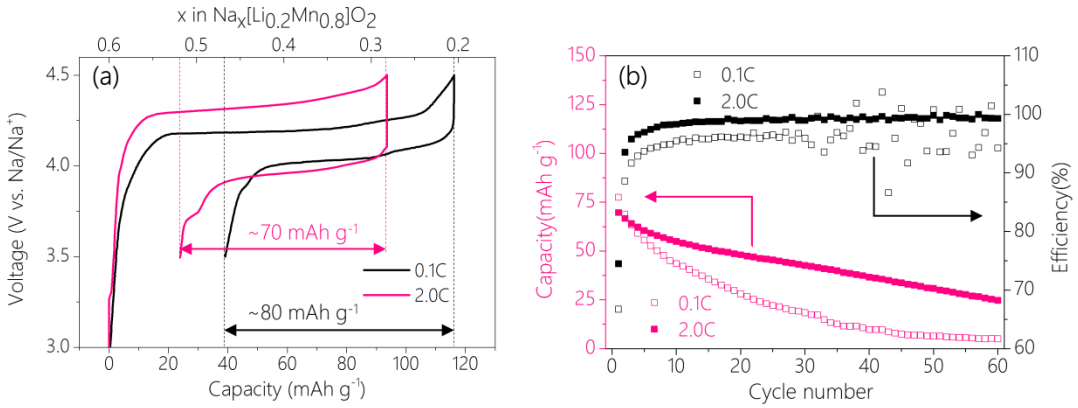

Figure 2 Electrochemical performance of $Na_{0.6}[Li_{0.2}Mn_{0.8}]O_2$. (a) The charge/discharge curves at different current rate of 0.1C (10 mAg^{-1}) and 2.0C (200 mAg^{-1}) within the voltage range of 3.5-4.5 V versus Na/Na^+ for $Na_{0.6}Li_{0.2}Mn_{0.8}O_2$ and (b)the comparison of discharge capacity and coulombic efficiency versus cycle number at 0.1C and 2.0C rate.

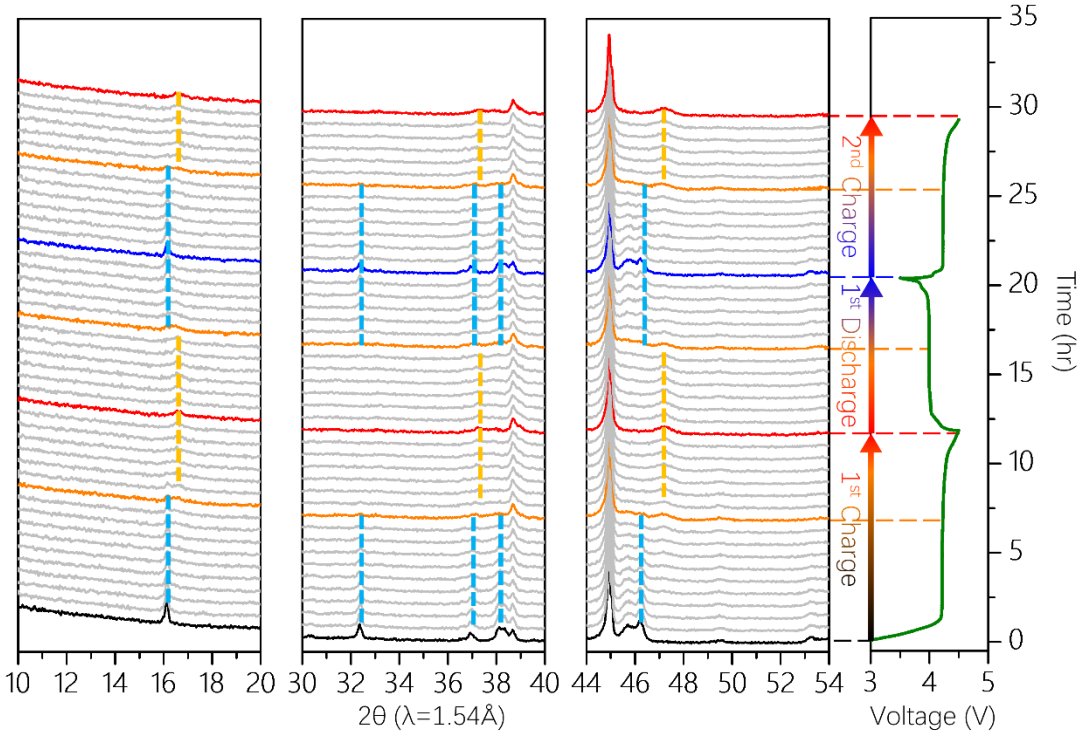

Figure 3 Crystal structural evolution of $Na_{0.6}[Li_{0.2}Mn_{0.8}]O_2$. The collect XRD

patterns of $Na_{0.6}[Li_{0.2}Mn_{0.8}]O_2$/Na cell charged and discharged at a rate of C/20.

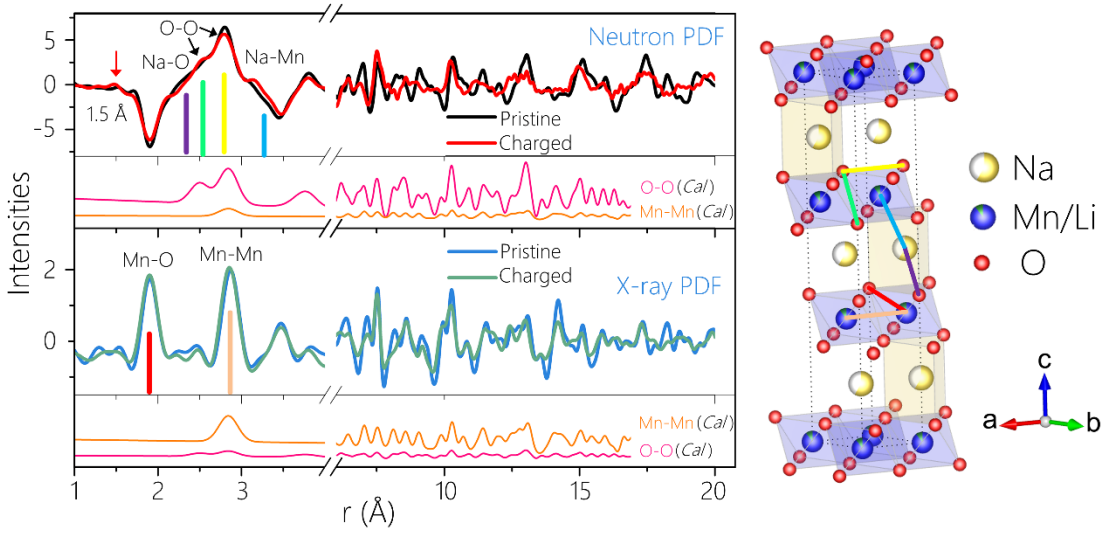

Figure 4 Detection of local structural changes upon desodiation. Comparison of X-ray and neutron PDF of $Na_{0.6}[Li_{0.2}Mn_{0.8}]O_2$ collected at pristine and charged state (4.5V). The representative peaks corresponding to such as the first coordinating O-O, Mn-O and Mn-Mn bonding are labelled. Due to the relative larger neutron scattering length of oxygen compared with that of manganese, the changes of the oxygen network associated with oxidation of oxygen anions is able to be detected by neutron PDF.

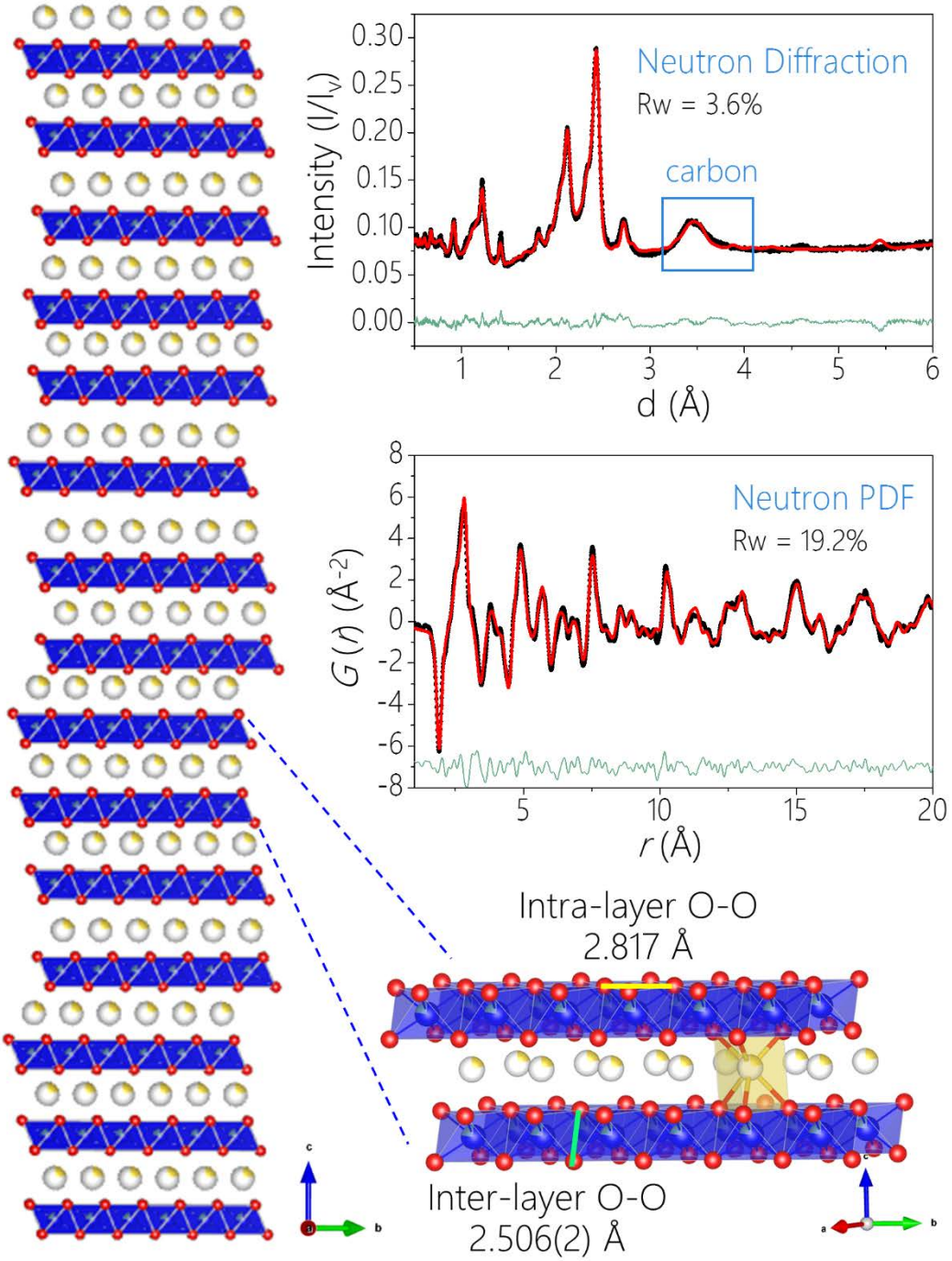

Figure 5 Structure of the initial charged (4.5 V) sample. Left, the refined 15 layer supercell model for the 4.5V charged $Na_{0.2}Li_{0.2}Mn_{0.8}O_2$. Right, refinement results of the neutron diffraction data and PDF data using the structural model shown on the left. Local coordination environments of O and residual Na are shown as enlarged figure on the bottom.

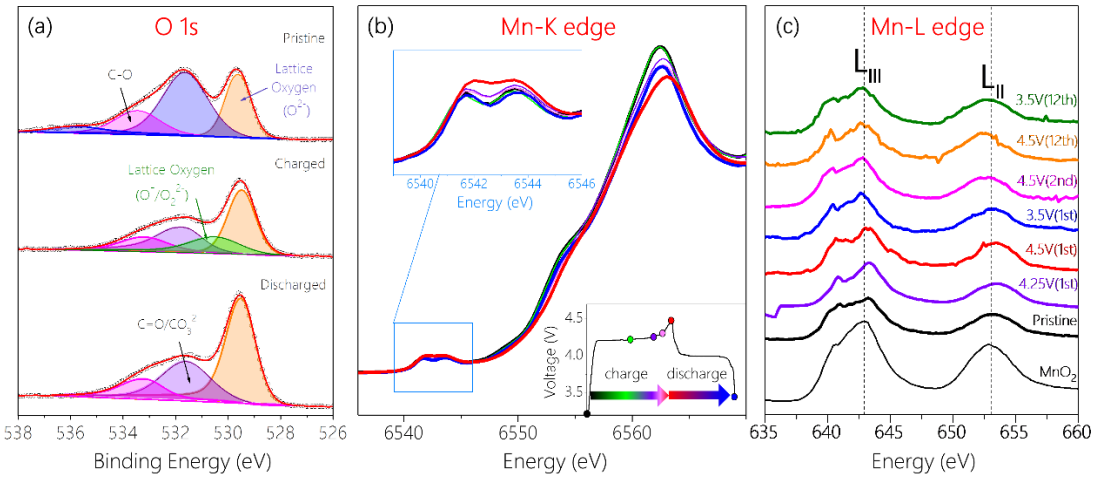

Figure 6 Spectroscopic investigation of charge compensation mechanism of $Na_{0.6}[Li_{0.2}Mn_{0.8}]O_2$ during sodium storage. (a) The XPS O1s spectra collected for the pristine sample and samples charged to 4.5V, and discharged to 3.5V. The peak at 530.5eV appears/disappears at charged/discharged states, indicating the redox activity of lattice oxygen; (b) Mn K-edge and (c) Mn L-edge spectra of $Na_{0.6}[Li_{0.2}Mn_{0.8}]O_2$ collected at different charge and discharge states. The Mn ions remain at Mn^{4+} in the voltage range between 3.5V and 4.5V during Na^+ de-intercalation/intercalation.

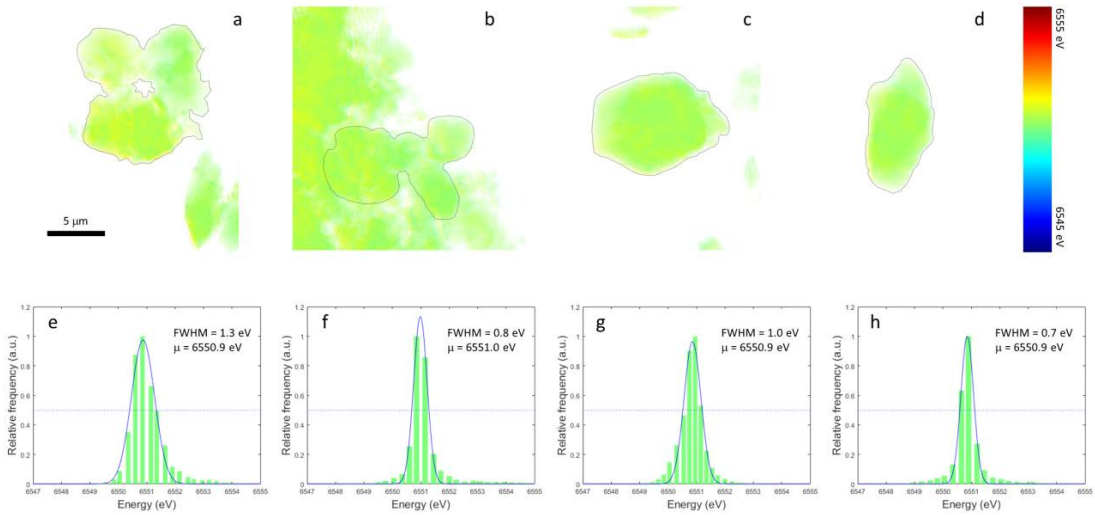

Figure 7 2D nanoscale mapping of Mn oxidation states in particles with different cycling history. The similarity in the overall color of the particles shown in the top row (panels (a) pristine, (b) charged at 4.5 V, (c) discharged at 3.5 V, and (d) discharged at 3.5V after 30 cycles) suggests the homogeneity of the Mn's oxidation states regardless of the SOC and the cycling history up to 30 cycles. The corresponding histograms of

the Mn oxidation state over the highlighted particles are shown in the bottom row.

1 Mizushima, K., Jones, P. C., Wiseman, P. J. & Goodenough, J. B. LixCoO 2 (0<x˜l): A NEW CATHODE MATERIAL FOR BATTERIES OF HIGH ENERGY DENSITY. *Mater. Res. Bull.* **15**, 783-789 (1980).

2 Ohzuku, T., Ueda, A., Nagayama, M., Iwakoshi, Y. & Komori, H. Comparative study of LiCoO2, LiNi12Co12O2 and LiNiO2 for 4 volt secondary lithium cells. *Electrochimica Acta* **38**, 1159-1167, doi:http://dx.doi.org/10.1016/0013-4686(93)80046-3 (1993).

3 Lu, Z., MacNeil, D. D. & Dahn, J. R. Layered Li[Ni[sub x]Co[sub 1−2x]Mn[sub x]]O[sub 2] Cathode Materials for Lithium-Ion Batteries. *Electrochemical and Solid-State Letters* **4**, A200, doi:10.1149/1.1413182 (2001).

4 Li, Y. *et al.* Advanced sodium-ion batteries using superior low cost pyrolyzed anthracite anode: towards practical applications. *Energy Storage Materials* **5**, 191-197, doi:10.1016/j.ensm.2016.07.006 (2016).

5 Li, Y. *et al.* Recent advances of electrode materials for low-cost sodium-ion batteries towards practical application for grid energy storage. *Energy Storage Materials* **7**, 130-151, doi:10.1016/j.ensm.2017.01.002 (2017).

6 Lee, J. *et al.* Unlocking the potential of cation-disordered oxides for rechargeable lithium batteries. *Science* **343**, 519-522, doi:10.1126/science.1246432 (2014).

7 Sathiya, M. *et al.* Reversible anionic redox chemistry in high-capacity layered-oxide electrodes. *Nature materials* **12**, 827-835, doi:10.1038/nmat3699 (2013).

8 Lu, Z., Beaulieu, L. Y., Donaberger, R. A., Thomas, C. L. & Dahn, J. R. Synthesis, Structure, and Electrochemical Behavior of Li[Ni[sub x]Li[sub 1/3−2x/3]Mn[sub 2/3−x/3]]O[sub 2]. *Journal of The Electrochemical Society* **149**, A778, doi:10.1149/1.1471541 (2002).

9 Park, Y. J., Hong, Y.-S., Wu, X., Ryu, K. S. & Chang, S. H. Structural investigation and electrochemical behaviour of Li[NixLi(1/3−2x/3)Mn(2/3−x/3)]O2 compounds by a simple combustion method. *Journal of Power Sources* **129**, 288-295, doi:10.1016/j.jpowsour.2003.11.024 (2004).

10 Nayak, P. K., Grinblat, J., Levi, M., Markovsky, B. & Aurbach, D. Structural and Electrochemical Evidence of Layered to Spinel Phase Transformation of Li and Mn Rich Layered Cathode Materials of the Formulae xLi[Li1/3Mn2/3]O2.(1-x)LiMn1/3Ni1/3Co1/3O2 (x = 0.2, 0.4, 0.6) upon Cycling. *Journal of the Electrochemical Society* **161**, A1534-A1547, doi:10.1149/2.0101410jes (2014).

11 Shunmugasundaram, R., Senthil Arumugam, R. & Dahn, J. R. High Capacity Li-Rich Positive Electrode Materials with Reduced First-Cycle Irreversible Capacity Loss. *Chemistry of Materials* **27**, 757-767, doi:10.1021/cm504583y (2015).

12 Lu, Z. & Dahn, J. R. Understanding the Anomalous Capacity of Li/Li[Ni[sub x]Li[sub (1/3−2x/3)]Mn[sub (2/3−x/3)]]O[sub 2] Cells Using In Situ X-Ray Diffraction and Electrochemical Studies. *Journal of The Electrochemical Society* **149**, A815, doi:10.1149/1.1480014 (2002).

13 Yoon, W.-S. *et al.* Combined NMR and XAS Study on Local Environments and Electronic Structures of Electrochemically Li-Ion Deintercalated Li[sub 1−x]Co[sub 1/3]Ni[sub 1/3]Mn[sub 1/3]O[sub 2] Electrode System. *Electrochemical and Solid-State Letters* **7**, A53, doi:10.1149/1.1643592 (2004).

14 Koga, H. *et al.* Reversible Oxygen Participation to the Redox Processes Revealed for Li1.20Mn0.54Co0.13Ni0.13O2. *Journal of the Electrochemical Society* **160**, A786-A792,

doi:10.1149/2.038306jes (2013).

15 McCalla, E. *et al.* Visualization of O-O peroxo-like dimers in high-capacity layered oxides for Li-ion batteries. *Science* **350**, 1521-1516 (2015).

16 Grimaud, A., Hong, W. T., Shao-Horn, Y. & Tarascon, J. M. Anionic redox processes for electrochemical devices. *Nature materials* **15**, 121-126, doi:10.1038/nmat4551 (2016).

17 Luo, K. *et al.* Charge-compensation in 3d-transition-metal-oxide intercalation cathodes through the generation of localized electron holes on oxygen. *Nature chemistry* **8**, 684-691, doi:10.1038/nchem.2471 (2016).

18 Seo, D. H. *et al.* The structural and chemical origin of the oxygen redox activity in layered and cation-disordered Li-excess cathode materials. *Nature chemistry* **8**, 692-697, doi:10.1038/nchem.2524 (2016).

19 Armstrong, A. R. *et al.* Demonstrating Oxygen Loss and Associated Structural Reorganization in the Lithium Battery Cathode Li[Ni0.2Li0.2Mn0.6]O2. **128**, 8694-8698 (2006).

20 Yoon, W.-S. *et al.* Investigation of the Charge Compensation Mechanism on the Electrochemically Li-Ion Deintercalated Li1-Co1/3Ni1/3Mn1/3O2 Electrode System by Combination of Soft and Hard X-ray Absorption Spectroscopy. *J. AM. CHEM. SOC.* **127**, 17479-17487 (2005).

21 Du, K. *et al.* Exploring reversible oxidation of oxygen in a manganese oxide. *Energy Environ. Sci.* **9**, 2575-2577, doi:10.1039/c6ee01367h (2016).

22 de la Llave, E. *et al.* Improving Energy Density and Structural Stability of Manganese Oxide Cathodes for Na-Ion Batteries by Structural Lithium Substitution. *Chemistry of Materials* **28**, 9064-9076, doi:10.1021/acs.chemmater.6b04078 (2016).

23 Breger, J. *et al.* Short- and Long-Range Order in the Positive Electrode Material, Li(NiMn)0.5O2: A Joint X-ray and Neutron Diffraction, Pair Distribution Function Analysis and NMR Study. *J. AM. CHEM. SOC.* **127**, 7529-7537 (2005).

24 Bréger, J., Kang, K., Cabana, J., Ceder, G. & Grey, C. P. NMR, PDF and RMC study of the positive electrode material Li(Ni0.5Mn0.5)O2 synthesized by ion-exchange methods. *Journal of Materials Chemistry* **17**, 3167, doi:10.1039/b702745a (2007).

25 Yamakawa, N., Jiang, M., Key, B. & Grey, C. P. Identifying the Local Structures Formed during Lithiation of the Conversion Material, Iron Fluoride, in a Li Ion Battery: A Solid-State NMR, X-ray Diffraction, and Pair Distribution Function Analysis Study. *J. AM. CHEM. SOC.* **131**, 10525-10536 (2009).

26 Key, B., Morcrette, M., Tarascon, J.-M. & Grey, C. P. Pair Distribution Function Analysis and Solid State NMR Studies of Silicon Electrodes for Lithium Ion Batteries: Understanding the (De)lithiation Mechanisms. *J. AM. CHEM. SOC* **133**, 503-512 (2011).

27 Liu, J., Huq, A., Moorhead-Rosenberg, Z., Manthiram, A. & Page, K. Nanoscale Ni/Mn Ordering in the High Voltage Spinel Cathode LiNi0.5Mn1.5O4. *Chemistry of Materials* **28**, 6817-6821, doi:10.1021/acs.chemmater.6b02946 (2016).

28 Zhou, Y.-N. *et al.* High-Rate Charging Induced Intermediate Phases and Structural Changes of Layer-Structured Cathode for Lithium-Ion Batteries. *Advanced Energy Materials* **6**, 1600597, doi:10.1002/aenm.201600597 (2016).

29 Komaba, S. *et al.* Study on the reversible electrode reaction of Na(1-x)Ni(0.5)Mn(0.5)O2 for a rechargeable sodium-ion battery. *Inorg Chem* **51**, 6211-6220, doi:10.1021/ic300357d (2012).

30 Xu, Y. *et al.* Structural integrity—Searching the key factor to suppress the voltage fade of Li-rich

layered cathode materials through 3D X-ray imaging and spectroscopy techniques. *Nano Energy* **28**, 164-171, doi:10.1016/j.nanoen.2016.08.039 (2016).

31 Koga, H. *et al.* Different oxygen redox participation for bulk and surface: A possible global explanation for the cycling mechanism of Li1.20Mn0.54Co0.13Ni0.13O2. *Journal of Power Sources* **236**, 250-258, doi:10.1016/j.jpowsour.2013.02.075 (2013).

32 Chen, H. & Islam, M. S. Lithium Extraction Mechanism in Li-Rich Li2MnO3 Involving Oxygen Hole Formation and Dimerization. *Chemistry of Materials* **28**, 6656-6663, doi:10.1021/acs.chemmater.6b02870 (2016).

33 Chen, S. & Wang, L.-W. Double-hole-induced oxygen dimerization in transition metal oxides. *Physical Review B* **89**, doi:10.1103/PhysRevB.89.014109 (2014).

34 Liu, J. *et al.* Ionic Conduction in Cubic Na3TiP3O9N, a Secondary Na-Ion Battery Cathode with Extremely Low Volume Change. *Chemistry of Materials* **26**, 3295-3305, doi:10.1021/cm5011218 (2014).

35 Liu, J. *et al.* Quantification of Honeycomb Number-Type Stacking Faults: Application to Na3Ni2BiO6 Cathodes for Na-Ion Batteries. *Inorg Chem* **55**, 8478-8492, doi:10.1021/acs.inorgchem.6b01078 (2016).

36 Coelho, A. A., Chater, P. A. & Kern, A. Fast synthesis and refinement of the atomic pair distribution function. *Journal of Applied Crystallography* **48**, 869-875, doi:10.1107/s1600576715007487 (2015).

37 Neuefeind, J., Feygenson, M., Carruth, J., Hoffmann, R. & Chipley, K. K. The Nanoscale Ordered MAterials Diffractometer NOMAD at the Spallation Neutron Source SNS. *Nuclear Instruments and Methods in Physics Research Section B: Beam Interactions with Materials and Atoms* **287**, 68-75, doi:10.1016/j.nimb.2012.05.037 (2012).

38 Tohyama, T. *et al.* Valence Change of A′ -Site Mn by A-Site Doping in La1 − xNaxMn3Ti4O12. *Chemistry of Materials* **25**, 178-183, doi:10.1021/cm303182u (2013).

39 Gordon, R., Bender, R. & Herman, G. T. Algebraic Reconstruction Techniques (ART) for three-dimensional electron microscopy and X-ray photography. *Journal of Theoretical Biology* **29**, 471-481, doi:http://dx.doi.org/10.1016/0022-5193(70)90109-8 (1970).

40 Guan, H. & Gordon, R. A projection access order for speedy convergence of ART (algebraic reconstruction technique): a multilevel scheme for computed tomography. *Phys. Med. Biol.* **39**, 2005-2022 (1994).

41 Harris, W. M. *et al.* Nondestructive volumetric 3-D chemical mapping of nickel-sulfur compounds at the nanoscale. *Nanoscale* **4**, 1557-1560, doi:10.1039/c2nr11690a (2012).

42 Liu, Y. *et al.* TXM-Wizard: a program for advanced data collection and evaluation in full-field transmission X-ray microscopy. *Journal of Synchrotron Radiation* **19**, 281-287, doi:doi:10.1107/S0909049511049144 (2012).

43 Andrews, J. C. & Weckhuysen, B. M. Hard X-ray spectroscopic nano-imaging of hierarchical functional materials at work. *Chemphyschem : a European journal of chemical physics and physical chemistry* **14**, 3655-3666, doi:10.1002/cphc.201300529 (2013).